ACS NANO

www.acsnano.org

ARTICLE

Toward Mass Production of Transition Metal Dichalcogenide Solar Cells: Scalable Growth of Photovoltaic-Grade Multilayer WSe_2 by Tungsten Selenization

Kathryn M. Neilson,[‡‡] Sarallah Hamtaei,[‡‡] Koosha Nassiri Nazif,[‡‡] Joshua M. Carr, Sepideh Rahimisheikh, Frederick U. Nitta, Guy Brammertz, Jeffrey L. Blackburn, Joke Hadermann, Krishna C. Saraswat, Obadiah G. Reid, Bart Vermang, Alwin Daus, and Eric Pop*

Cite This: *ACS Nano* 2024, 18, 24819–24828

Read Online

ACCESS | Metrics & More | Article Recommendations | Supporting Information

ABSTRACT: **Semiconducting transition metal dichalcogenides (TMDs) are promising for high-specific-power photovoltaics due to their desirable band gaps, high absorption coefficients, and ideally dangling-bond-free surfaces. Despite their potential, the majority of TMD solar cells to date are fabricated in a nonscalable fashion, with exfoliated materials, due to the lack of high-quality, large-area, multilayer TMDs. Here, we present the scalable, thickness-tunable synthesis of multilayer WSe_2 films by selenizing prepatterned tungsten with either solid-source selenium at 900 °C or H_2Se precursors at 650 °C. Both methods yield photovoltaic-grade, wafer-scale WSe_2 films with a layered van der Waals structure and superior characteristics, including charge carrier lifetimes up to 144 ns, over 14× higher than those of any other large-area TMD films previously demonstrated. Simulations show that such carrier lifetimes correspond to ∼22% power conversion efficiency and ∼64 W g^{-1} specific power in a packaged solar cell, or ∼3 W g^{-1} in a fully packaged solar module. The results of this study could facilitate the mass production of high-efficiency multilayer WSe_2 solar cells at low cost.**

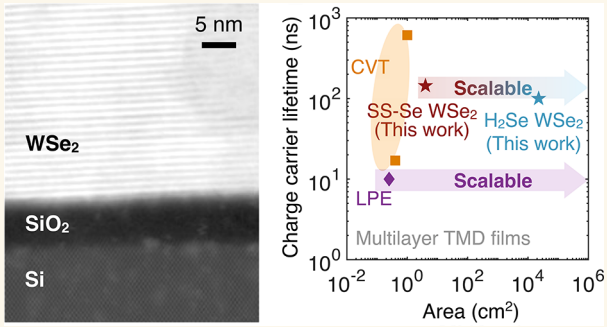

KEYWORDS: *transition metal dichalcogenides, solar cells, selenization, photovoltaic, carrier lifetime*

INTRODUCTION

Semiconducting transition metal dichalcogenides (TMDs), e.g., MoS_2 and WSe_2, offer excellent electronic and optical properties for use in a variety of applications, from nanoelectronics to photovoltaics. These include good charge carrier mobility in atomically thin (sub-1 nm) layers, ultrahigh optical absorption coefficients, near-ideal band gaps for solar energy harvesting, surfaces without dangling bonds, and facile integration on rigid and flexible substrates.[1−4] In particular, TMDs hold great promise in high-specific-power (i.e., high-power per-weight) applications, such as energy harvesting in high-altitude drones and wearable electronics, where lightweight and high power output are desired.[5−7] These emerging photovoltaic markets are growing at a rapid pace, potentially exceeding $100 billion by 2027.[5]

Recent studies have shown that optimally designed thin (<100 nm) TMD solar cells made of sulfides or selenides could achieve ∼25% power conversion efficiency (PCE) in a single-junction structure[2,8] and ∼32% PCE in a TMD-silicon tandem structure,[9] on par with current perovskite-silicon tandem solar cells.[10] As a result, single-junction TMD solar cells can offer excellent specific power (power-per-weight) greater than 40 W g^{-1}, about 10× higher than that of established thin-film solar cell technologies such as cadmium telluride (CdTe), copper indium gallium selenide (CIGS), amorphous silicon (a-Si), and III-V materials.[6,7,11] In addition, while thin-film solar cell technologies face challenges such as high cost (III−V single and multijunction cells), low durability (perovskite, organic,

Received: March 15, 2024
Revised: July 12, 2024
Accepted: July 25, 2024
Published: August 23, 2024

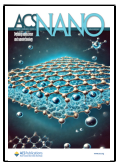

https://doi.org/10.1021/acsnano.4c03590
ACS Nano 2024, 18, 24819−24828

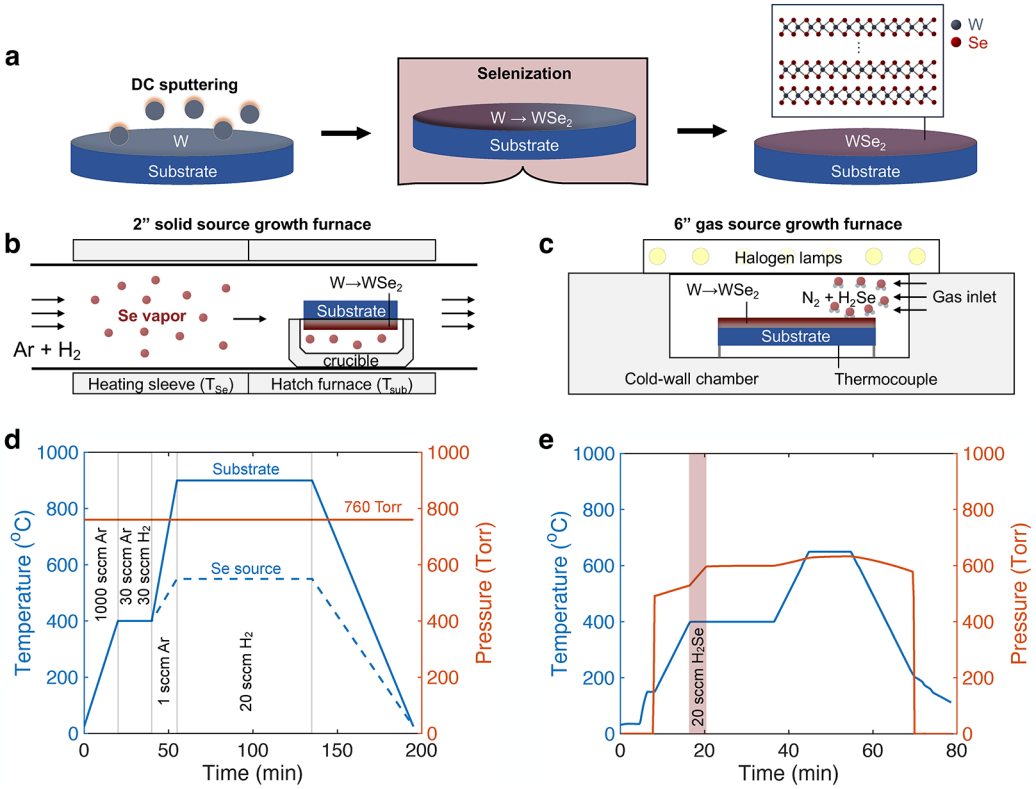

Figure 1. Scalable growth of WSe_2 by selenization of tungsten (W) using solid-source selenium (SS-Se) or H_2Se precursors. (a) Selenization process flow. Furnace setups for (b) SS-Se and (c) H_2Se selenization processes. Optimized temperature and pressure vs time for (d) SS-Se and (e) H_2Se processes. The dashed and solid blue lines in (d) correspond to T_{Se} and T_{sub} in (b), respectively. H_2Se selenization growth is done at a lower thermal budget (temperature) and pressure compared to that of SS-Se. Flow is continuously supplied for SS-Se (d) versus the finite introduction of H_2Se (e). Initial pressure changes in H_2Se selenization growths are achieved by N_2 gas.

and dye-sensitized photovoltaics), and the use of rare (CIGS) or toxic materials (CdTe, PbS quantum dot, and lead-based perovskite), TMD solar cells provide a potentially low-cost, durable, eco-friendly, and biocompatible solution which could reach future large-scale adoption.

The majority of TMD synthesis research over the past decade has been focused on monolayer (<1 nm thin) films, particularly for use in next-generation transistors. In contrast, high-quality TMD multilayers are most often obtained in a nonscalable fashion through the mechanical exfoliation of micron-scale flakes from bulk crystals grown by chemical vapor transport (CVT). Selenization, sulfurization, or tellurization of metallic precursor(s) could be employed as a low-cost method to synthesize TMD films at the industrial scale, similar to CIGS.[12] In this approach, the substrate size is, in principle, limited only by the furnace dimensions and can be easily scaled to larger areas with the use of industrial tools.

In practice, while sulfurization has achieved more uniform films, selenization and tellurization have proven to be more difficult. This has been mainly attributed to the lower chemical reactivity of selenium and tellurium, which requires the presence of a reducing agent when growing selenide and telluride films.[13,14] While synthesis by tellurization has made progress,[14] the band gaps of semiconducting tellurium-based TMDs are smaller (~0.7 eV) and less optimal for solar applications than those of selenides. On the other hand, previous studies on the selenization synthesis of WSe_2 films have shown suboptimal properties for photovoltaics, being either too thin,[15,16] too rough,[17] or suffering from morphological inhomogeneity.[18,19] The selenization process itself could also exceed 20 h, rendering it unfavorable from an industrial perspective.[20] An ideal film growth would have controllable thickness that is atomically smooth and oriented in the (001) plane with sufficiently large grain sizes and good charge carrier lifetimes.

Herein, we demonstrate the scalable synthesis of multilayer (15−30 nm thick) WSe_2 on up to 150 mm wafers by selenization of sputtered tungsten films using (1) solid-source selenium (SS-Se) at 900 °C and (2) low-thermal-budget H_2Se precursors at 650 °C in 1−2 h, leading to optimal characteristics for use as an absorber layer in ultrathin high-specific-power solar cells. At such thicknesses, WSe_2 has a band gap of 1.2−1.3 eV, which is near-ideal for solar energy harvesting under both the AM0 and AM1.5G spectra. Additionally, our approach results in films with superior characteristics compared to previous selenization reports,[16−21] including van der Waals (vdW)-layered structure, smooth and uniform surfaces, grain sizes comparable to the film thickness, Hall mobilities up to 8 $cm^2\ V^{-1}\ s^{-1}$, and minority carrier lifetimes up to 144 ns, over 14× greater than that of previous reports on large-area TMD films prepared by liquid exfoliation.[19] Here, we specifically focus on the absorber material due to the separate challenges associated with solar cell design;[22] however, with improved contacts and doping, we estimate these WSe_2 films can provide efficiency up to 22.3% in an optimized solar cell design. More importantly, upon integration on ultrathin flexible substrates, such solar cells are calculated to provide a specific power of ~64 W g^{-1} in a

https://doi.org/10.1021/acsnano.4c03590
ACS Nano 2024, 18, 24819−24828

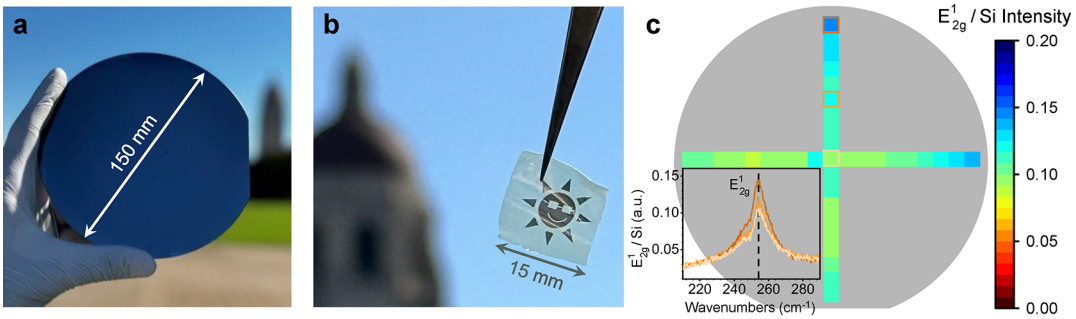

Figure 2. Versatility and scalability of the selenization growth method. (a) Photograph of a WSe_2 film uniformly grown by H_2Se on a 150 mm wafer. The film size is only limited by the substrate and furnace dimensions. (b) WSe_2 film obtained from SS-Se selenization of prepatterned W, transferred onto a flexible, lightweight polyimide substrate. (Selenization can be performed both on blanket-deposited and patterned W.) Due to their vdW nature, such selenized films can be easily transferred to other rigid or flexible substrates. (c) Raman spectroscopy shows little change of the E^1_{2g} peak intensity (normalized by the Si peak) over two orthogonal wafer diameters, indicating wafer-scale WSe_2 uniformity. Note that the measured data spans a narrower range (0.09−0.14) than the color bar (0−0.20), illustrating the growth uniformity. The inset shows normalized Raman spectra of WSe_2 at three spots marked by squares along the vertical scan.

packaged cell, over 10× higher than that of established thin-film solar cell technologies.[11] Fully packaged modules, which include considerations such as interconnect weight and encapsulation, show a specific power of up to 3 W g^{-1}, approximately 5× higher than the record of 0.7 W g^{-1}, demonstrated in a multijunction III−V-based solar module.[5]

WSe_2 GROWTH BY SELENIZATION OF TUNGSTEN

To prepare the WSe_2 film, we sputter 5−10 nm of tungsten using a DC source (Kurt J. Lesker) at 50 W onto ∼500 μm-thick silicon substrates at a pressure of 10 mTorr and an argon (Ar) flow rate of 50 sccm (Figure 1a) to provide an optimal film porosity.[18] (See Supporting Information Figure S1 for further discussion on the effect of sputtering pressure on growth quality.) These films can either be prepatterned (via lithography and lift-off) or blanket-deposited. The tungsten films are then selenized into multilayer (15−30 nm) WSe_2 by either SS-Se selenization at 900 °C or by hydrogen selenide (H_2Se) at 650 °C, as shown in Figure 1b−e. The final film thickness is mainly controlled by the starting thickness of the sputtered W, with the caveat that very thin starting films (<a few nm) require significantly shorter growth times to remain as continuous films versus as islands. The growth rate is relatively consistent after a W thickness of a few nm for a final film thickness of approximately 2.1 times the starting thickness. H_2Se provides a potentially more homogeneous selenization and higher chemical reactivity, therefore lowering the synthesis temperature and thermal budget. SS-Se can be processed at higher temperatures with higher quality but with more difficulty in process repeatability and scalability due to the use of solid-source selenium pellets. Nevertheless, both routes have shown promise to produce large-area, high-quality films in chalcogenide technologies (for example, CIGS[23,24]).

SS-selenization is carried out in a two-zone tube furnace (Figure 1b), where Se pellets are placed in a crucible upstream, subsequently vaporized at elevated temperatures, and then transported by carrier gas (Ar) to the main heating zone of the furnace containing the substrate. The substrate is placed face-down on a crucible to prevent sublimation of stoichiometric transition metal films at high temperatures,[25] and both zones are heated to 400 °C for 20 min (Figure 1d). Subsequently, the Se zone is heated to 550 °C, and the substrate is heated to 900 °C for 1 h. Given that the as-deposited W film may have natural surface oxidation before it is placed in the furnace, we flow additional H_2 gas to convert this surface into a more reactive WO_{3-x} form.[26] The furnace is then left to naturally cool to room temperature.

For the growth with H_2Se, a rapid thermal annealing tool is employed with N_2 and H_2Se as process gases (Figure 1c). The sample faces up on a silicon carbide (SiC)-coated graphite susceptor. The growth is done by a two-stage anneal (Figure 1e); the chamber is filled with 488 Torr of N_2 base pressure, which is heated up to 400 °C. The sample is then annealed for 20 min, with 75 Torr of diluted H_2Se gradually fed into the chamber during the first 4 min, at 20 sccm. The flow rate is chosen to provide sufficient carrier gas while allowing for the films to remain planar on the substrate (versus island formation or delamination in situ). The chamber is subsequently heated to 650 °C, where the sample is held for 10 min before cooling to room temperature. Immediately after the two annealing stages (at 400 and 650 °C), the chamber pressure is 600 and 638 Torr, respectively. All heat-up and cool-down ramps are set to 0.5 °C/s.

Figure 2 shows the versatility and scalability of the selenization growth method. Selenization of W leads to multilayer WSe_2 films whose thickness can be tuned by the amount of sputtered W. The substrate size is only limited by the furnace dimensions, which in our study are 50 mm for the solid-source selenization and 150 mm for the gas-source selenization (Figure 2a). Industrialized furnaces would enable growth on even larger substrates, i.e., 300 mm or greater. The WSe_2 films are highly uniform, with vdW structure, and can be easily transferred to other rigid or flexible substrates, e.g., to build flexible, high-specific-power solar cells.[11] For example, Figure 2b shows a prepatterned WSe_2 film transferred onto a flexible, lightweight polyimide (PI) substrate, and Figure 2c demonstrates the growth uniformity on a 150 mm wafer by displaying the highest intensity Raman peak (E^1_{2g}) of WSe_2 normalized to the silicon substrate below.

Material Characterization. Several characterization methods are used to assess the quality of the grown WSe_2 films. Initial scanning electron microscopy (SEM) images show smooth WSe_2 grown with H_2Se (Figure 3a). Energy-dispersive X-ray spectroscopy (EDS) is used to determine the Se-to-W ratio (Figure 3b,c) of the films either as-grown on silicon or after transfer to PI. EDS spectra are taken under a 5 kV acceleration voltage (Figure 3b) to ensure data acquisition at the surface. The measurement is first done at the edge of the

https://doi.org/10.1021/acsnano.4c03590
ACS Nano 2024, 18, 24819−24828

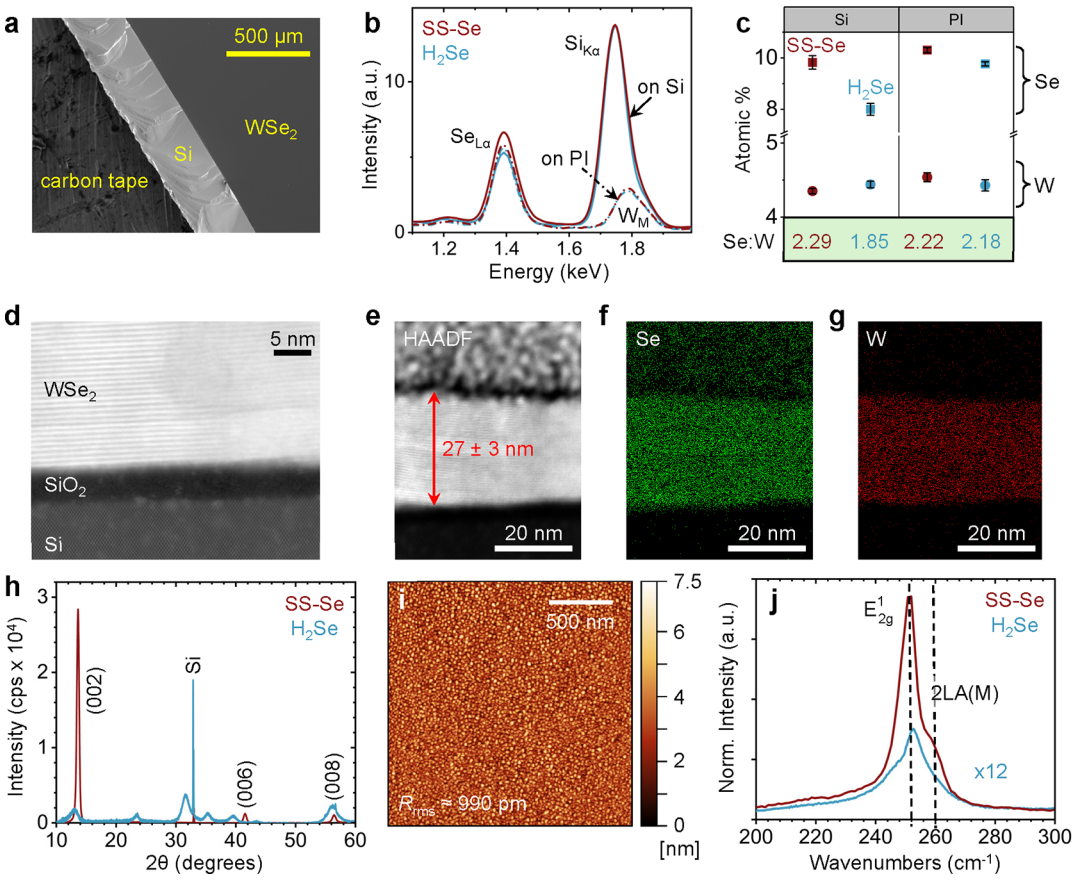

Figure 3. Material characterization of WSe_2. (a) H_2Se-grown films imaged under the scanning electron microscope at the edge of the chip; (b) resulting energy-dispersive X-ray spectra of WSe_2 as-grown on Si and transferred onto PI in order to deconvolute the W emission from the Si substrate; and (c) resulting Se/W ratio of approximately 2:1, as anticipated for a fully converted WSe_2 film. (d) HAADF-STEM cross-section of WSe_2 samples from SS-Se growth. (e) HAADF-STEM cross-section of the WSe_2 film with (f) Se and (g) W elemental mapping. The top layers are protective Pt/C coatings added during sample preparation. (h) XRD spectra of blanket films, measured on silicon. (i) Surface topography of H_2Se films measured by AFM. (j) Room-temperature Raman spectra of representative films on Si.

chip, because the smoothness of the films makes it difficult to focus near the center, followed by two more measurements at randomly chosen and wide-apart locations.

Supporting Information Table 1 summarizes the average and coefficient of variation between these three measurements on silicon (Si) and PI substrates for solid-source and H_2Se recipes, while Figure 3c illustrates the average and standard deviation for Se and W values as well as the Se/W ratio. For as-grown samples (on Si), there is a ∼20% discrepancy between the compositions of solid-source and H_2Se recipes. This is mainly a measurement artifact due to the proximity of the W_M and $Si_{K\alpha}$ peaks at 1.774 and 1.739 keV, respectively, which causes peak fitting errors when translating the EDS peaks to the atomic concentration. We avoided the Si peak by transferring WSe_2 films to a PI substrate. The EDS data from WSe_2 on PI substrates indicate very similar film compositions from each recipe (Figure 3c), with a discrepancy of ∼1% between the solid-source and H_2Se recipes, within the detection limit of EDS (1 atomic %). We also observe high spatial homogeneity for each recipe with a coefficient of variation below 3% for Se and W atomic percentages (see tight error bars in Figure 3c).

A transmission electron microscopy (TEM) cross-section (Figure 3d) confirms the vdW-layered nature of the as-grown SS-Se films. Comparing the interlayer distances with the WSe_2 structure in the ICSD database ($a = b = 3.28$ Å, $c = 12.96$ Å, $\alpha = \beta = 90°$, $\gamma = 120°$)[27] and considering the atomic numbers of the constituting elements, each bright line is a plane containing W atoms, sandwiched between two Se layers (see Figure 3d). The EDS results illustrated in Figure 3f,g show the elemental distribution in the lamella (additional elemental mapping of the films is available in Supporting Information Figure 3). Strong W and Se signals are seen atop the silicon substrate, confirming the elemental distribution in the film. Additionally, the lamella is smooth, as the atomic force microscopy (AFM) image shows a root-mean-square roughness on the order of 1 nm (Figure 3i).

2θ–ω X-ray diffraction (XRD) scans verify the crystallinity of the selenized films, and the full-width at half-maximum is used to estimate the grain size using the Scherrer equation.[28] The presence of only (00l) out-of-plane peaks for SS-Se WSe_2 in Figure 3h demonstrates that the films are layered with alternating vdW gaps and undetectable out-of-plane crystallographic orientations, as verified by TEM (Figure 3d). Estimates based on the Scherrer equation indicate grain sizes of ∼17 nm for the SS-Se growth, comparable to the film thickness (see Supporting Information Table 2). On the other hand, WSe_2 films prepared with H_2Se have smaller average grain sizes of ∼8 nm, potentially due to the lower growth temperature and shorter anneal time (see Figure 1d,e).

Differences in the grain sizes of these films could be partially due to the higher synthesis temperature and longer anneal duration of SS-Se versus H_2Se (see Figure 1d,e); however, the

https://doi.org/10.1021/acsnano.4c03590
ACS Nano 2024, 18, 24819−24828

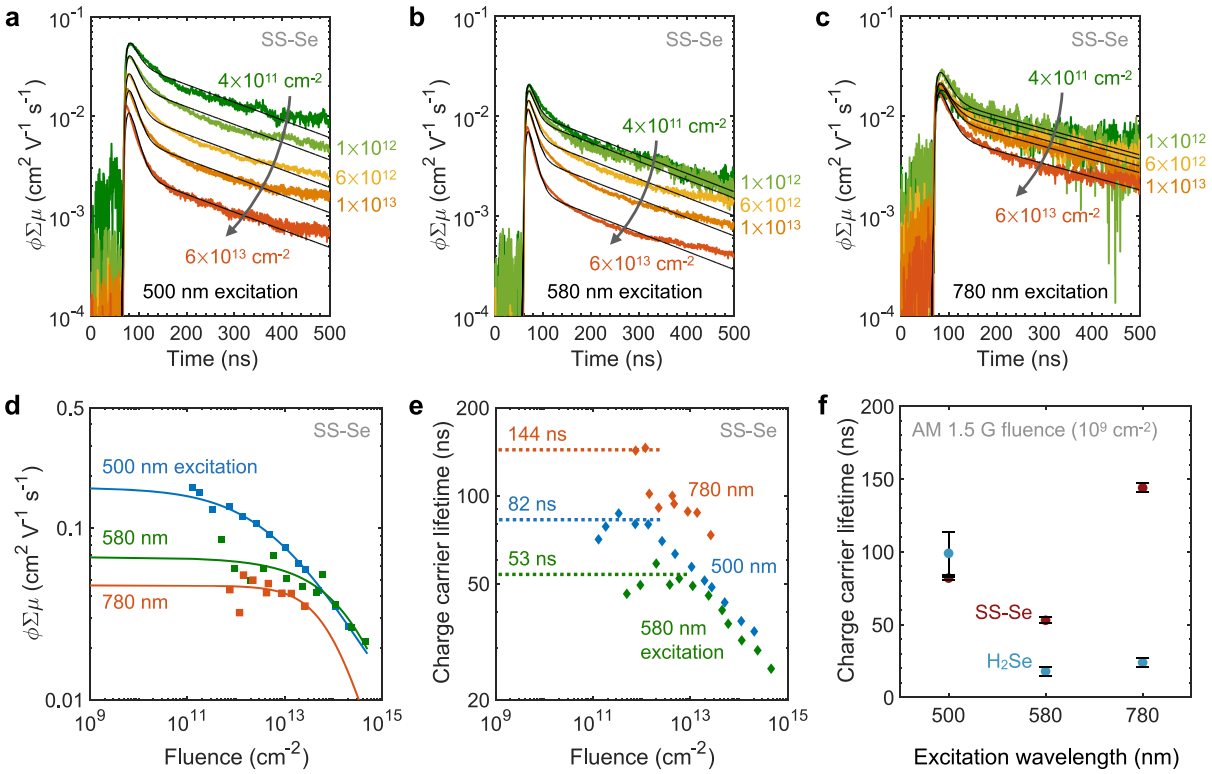

Figure 4. Flash-photolysis TRMC measurements. TRMC transients of WSe_2 grown by SS-Se at varying photon fluences (from ≈10^{11} to nearly 10^{14} cm^{-2}) for excitation wavelengths of (a) 500 nm, (b) 580 nm, and (c) 780 nm. Some transients are omitted for clarity. Solid lines represent a double exponential fit to the data. (d) Peak yield-mobility product vs fluence at the three excitation wavelengths (500, 580, and 780 nm) for WSe_2 grown by SS-Se. Square symbols are measurements; solid lines show a Dicker–Ferguson fit[40,41] to each data set, accounting for high-order recombination from exciton–exciton and exciton–charge quenching mechanisms. (e) Amplitude-weighted average charge carrier lifetime vs photon fluence at the same excitation wavelengths. Diamond symbols are measurements; dashed lines indicate charge carrier lifetimes averaged at low fluence, representing AM 1.5 G solar illumination (10^9 cm^{-2}). (f) Charge carrier lifetimes under AM 1.5 G fluence vs the three excitation wavelengths for WSe_2 films prepared by SS-Se (red) and H_2Se (blue) selenization. Error bars are approximated as the standard deviation of carrier lifetimes in the flat, plateaued regions of panel (e).

role of the precursor and gas flow differences also contributes to film quality. While H_2Se-grown films do show in-plane XRD peaks (Figure 3h), further optimization of growth parameters (such as growth promoters, carrier gas, or pressure optimization) could provide more ideal film orientation and larger grains as the partial pressure of Se during growth can determine the film orientation.[20]

We also display the Raman spectra of both selenization methods in Figure 3j, normalized to the Si peak of the substrate. These provide information about the vibrational modes, which correlate with the relative quality of the films.[29] Solid-source-grown films exhibit a distinct degenerate A_{1g}/E^1_{2g} peak and the 2LA(M) signature. WSe_2 films grown with H_2Se show an increased left shoulder of the E^1_{2g} peak, which could be due to a higher presence of defects in these films[30] or to degenerate peak splitting due to an increased presence of strain,[31] as indicated by the shifted out-of-plane (00l) peaks in the XRD spectra (Supporting Information Table 2).

Square WSe_2 samples measured by the van der Pauw method are used to determine the majority carrier type, density, and Hall mobility (fabrication details in Supporting Information Note 2). The films show p-type doping, with a hole density of ∼10^{17} cm^{-3} and an average Hall mobility of ∼5 cm^2 V^{-1} s^{-1} at room temperature (Supporting Information Figure 4). Across various samples, we measured Hall mobilities and hole densities up to 8.1 cm^2 V^{-1} s^{-1} and 4.2 × 10^{17} cm^{-3}, respectively. These are among the best mobility results reported to date for selenized WSe_2 (Supporting Information Table 2). SS-Se samples exhibit a tight distribution of Hall mobility and hole density, whereas H_2Se samples show wider variation (Supporting Information Figure 4). This could be explained by the mobility anisotropy in WSe_2 and the more varied orientation of WSe_2 layers observed in the H_2Se growths (Supporting Information Figure 2), causing sample-to-sample variation. In contrast, we note that SS-Se growths have better horizontal layering within the WSe_2 films.

Flash-Photolysis TRMC Measurement. The flash-photolysis time-resolved microwave conductivity (TRMC) method is adopted to determine the charge carrier lifetime in our selenized films, particularly as this dictates the efficiency limit in photovoltaic applications.[8] TRMC is a contactless microwave spectroscopy technique where a thin film sample is excited by a laser inside a resonant cavity, probed by microwave radiation, and measured as a function of time.[32] TRMC experiments provide the product of free-charge carrier yield and the sum of both electron and hole mobilities, known as the yield-mobility product $\phi\sum\mu = \phi(\mu_e + \mu_h)$, where ϕ is the yield of charges per photon, while μ_e and μ_h are the electron and hole mobilities, respectively. Both electrons and holes are produced by photoexcitation, but the degree to which carriers experience trap sites (and the precise energies of those traps) is unclear to date in TMDs. Thus, it is challenging to deconvolve $\phi\sum\mu$ to estimate the photogenerated carrier mobilities. Instead, we focus on the carrier lifetimes and

https://doi.org/10.1021/acsnano.4c03590
ACS Nano 2024, 18, 24819−24828

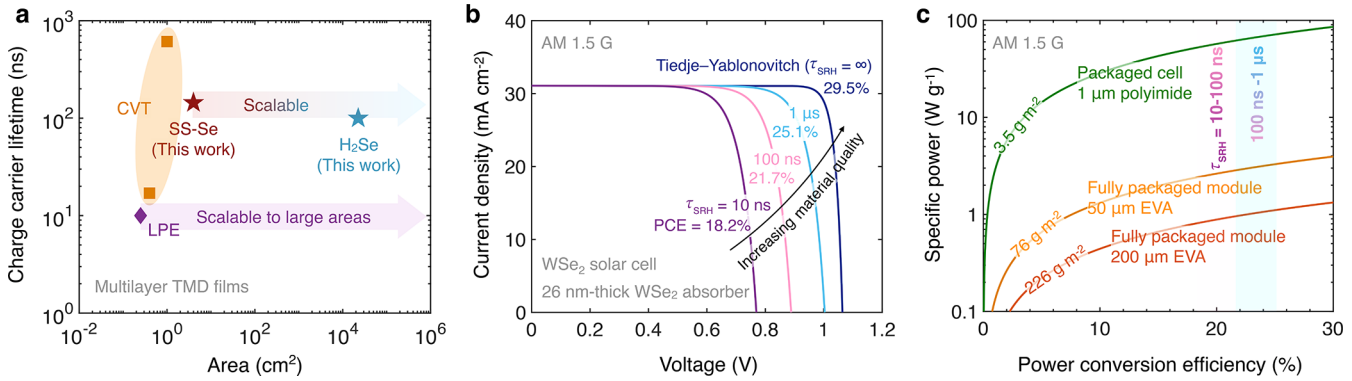

Figure 5. Projected performance of WSe_2 solar cells and modules. (a) Charge carrier lifetime and area of multilayer TMD films reported in the literature.[7,19,45] WSe_2 films grown by SS-Se and H_2Se selenization methods exhibit charge carrier lifetimes up to 144 ns, over 14× higher than those of liquid phase exfoliation (LPE) and on par with CVT. Note that the CVT method is not scalable to large areas (maximum crystal size of ~1 cm^2), whereas both selenization and LPE could be scaled. (b) Simulated current density vs voltage characteristics and power conversion efficiency (PCE) limits of 26 nm-thick WSe_2 solar cells at various synthesis quality levels, represented by the SRH recombination lifetime (τ_{SRH}). Our selenized WSe_2 films have carrier lifetimes up to 144 ns, corresponding to a PCE of 22.3% in an optimized design (Supporting Information Table 3). (c) Projected specific power of WSe_2 solar cells and modules. Upon integration on ultrathin flexible substrates, selenized WSe_2 solar cells can provide a specific power of ~64 W g^{-1} in a packaged cell, over 10× higher than that of established thin-film technologies.[11] Fully packaged modules, which account for interconnect weight and EVA (ethylene-vinyl acetate) encapsulation,[5] show a specific power up to 3 W g^{-1}, over 4× higher than the present record of 0.7 W g^{-1} in a multijunction III–V-based solar module.[5]

report the yield-mobility product (normalized by the fraction of absorbed photons) for the three excitation wavelengths.

To characterize TMD photoconductivity, we first examine the optical absorption and steady-state microwave conductivity (SSMC) action spectra[32−38] associated with films for which we could measure a sufficiently good response at low photon fluences (Supporting Information Figures 5 and 6). The optical absorption and SSMC action spectra provide the three excitation wavelengths (at 500, 580, and 780 nm) for the TRMC study as follows: (1) bulk transitions above the WSe_2 band gap (500 nm or 2.48 eV), (2) transitions into the B exciton (580 nm or 2.14 eV), and (3) transitions into the lowest A exciton (780 nm or 1.59 eV).[39] Figure 4a−c displays TRMC transients at varying fluences for the SS-Se films at the three excitation wavelengths. Figure 4d,e shows the peak $\phi\sum\mu$ vs fluence and the amplitude-weighted average carrier lifetimes vs photon fluence, respectively. Figure 4f displays carrier lifetimes in WSe_2 films obtained from both SS-Se (red) and H_2Se (blue) growth methods at a fluence of 10^9 cm^{-2}, for AM 1.5 G solar illumination. (Lifetimes are extrapolated from the average plateaus at low fluence in Figure 4e.)

Data summarized in Figure 4d,e show that both the yield-mobility product and the carrier lifetimes depend on fluence for the 500 and 580 nm excitations, but the excitation at 780 nm yields less fluence-dependence. This is explained by the different initial excitation energies with respect to the WSe_2 band gap, i.e., the bulk and B exciton energies (2.48 and 2.14 eV, i.e., 500 and 580 nm), which are above the WSe_2 optical gap (1.59 eV or 780 nm) and have overall lower Coulomb binding energies. Higher energy excitations (580 vs 780 nm, Figure 4d) lead to a greater yield of free charges, assuming that the mobility is equal in both cases. This trend suggests either that the exciton binding energy decreases as the excitation energy increases or that the relaxation process from higher energies to the minimum optical transition allows for more excitons to dissociate. However, the 500 nm excitations produce charges with a longer lifetime than 580 nm, despite their higher charge density. This unusual trend in lifetime could be due to defect sites facilitating charge separation, which are only made accessible by higher energy excitations, meaning that different types of defects could dominate the 500 vs 580 nm charge separation and recombination.

As shown in Figure 4f, SS-Se films tend to have carrier lifetimes higher than those of H_2Se samples, with these results being the first of their kind in selenized WSe_2 films, to our knowledge. This could be related to the larger grain size in WSe_2 films grown by SS-Se (17 vs 8 nm; see Supporting Information Table 2). Selenization on textured substrates, such as in CIGS,[42] may allow for even larger grain sizes and subsequently larger lifetimes. The carrier lifetime of 144 ns measured in this work is over 14× higher than that of previous demonstrations of scalable, large-area TMD films (up to 10 ns in liquid exfoliated WS_2),[19] as shown in Figure 5a. Our higher carrier lifetimes can be attributed to the vdW-layered structure and large grain size of our selenized films. Carrier lifetimes demonstrated here are on the same order of magnitude as the highest value reported for multilayer TMDs (611 ns for WS_2 grown by CVT,[7] a nonscalable synthesis method), as well as more established chalcogenides CdTe and CIGS,[43,44] confirming the high quality of our synthesis, particularly for photovoltaic applications (Figure 5a).

Projected Efficiency and Specific Power of WSe_2 Solar Cells and Modules. The ultimate performance limit of a single-junction solar cell is governed by the optoelectronic characteristics and synthesis quality of the absorber material. We perform realistic modeling of single-junction solar cell performance limits with WSe_2 absorber layers by accounting for both intrinsic and extrinsic properties (Figure 5). The model incorporates measured absorption data as well as radiative, Auger, and defect-assisted Shockley–Read–Hall (SRH) recombination, as described in our previous work.[8]

Figure 5b shows the simulated current density vs voltage and PCE limit of single-junction solar cells with 26 nm-thick WSe_2 absorber layers at various film quality levels, as represented by SRH recombination lifetimes (τ_{SRH}). This is the thickness of our selenized films and is also the thickness which maximizes

https://doi.org/10.1021/acsnano.4c03590
ACS Nano 2024, 18, 24819−24828

PCE[8] for lifetimes in the 10 ns to 1 μs range. Our model shows that τ_{SRH} of 10, 100, and 1 μs lead to PCE limits of 18.2, 21.7, and 25.1%, respectively (Figure 5b). In the absence of SRH recombination (defect-free WSe_2, $\tau_{SRH} = \infty$), these 26 nm thin WSe_2 solar cells reach a PCE of 29.5% at the Tiedje–Yablonovitch limit (or up to ~30.8% in films thicker than 100 nm[8]). Carrier lifetimes associated with radiative and Auger recombination in intrinsic or lightly doped multilayer WSe_2 are on the order of tens of microseconds.[8] Thus, measured carrier lifetimes below 1 μs correspond to SRH-dominated recombination, which is the case for our selenized WSe_2 films (Figure 4f). According to our realistic model, the selenized WSe_2 films in this study, which exhibit τ_{SRH} up to 144 ns, can achieve a PCE of 22.3% (Supporting Information Table 3) upon design optimization, which is on par with incumbent solar technologies such as Si, CdTe, and CIGS.[5]

More notably, after integration on ultrathin flexible substrates, selenized WSe_2 solar cells are expected to provide a specific power of ~64 W g^{-1} in a packaged cell (Figure 5c), over 10× higher than that of established thin-film solar cell technologies based on III-Vs, CdTe, and CIGS.[11] These packaged WSe_2 solar cells could be adopted in size-constrained, low-power applications for the Internet of Things (IoT) and wearable electronics. Higher-power applications such as satellites and electric vehicles require larger, fully packaged modules with higher areal weight densities due to additional interconnects and module encapsulation.[5] Such fully packaged WSe_2 modules are expected to have a specific power up to 3 W g^{-1}, over 4× higher than the present record of 0.7 W g^{-1} in multijunction III–V solar modules.[5]

CONCLUSIONS

We report scalable methods for large-area WSe_2 film synthesis with both solid-source and gaseous precursors for use as absorber layers in ultrathin high-specific-power solar cells. The films show vdW-layered structure and grain sizes on the order of the film thickness (17 nm). We report some of the highest Hall mobilities to date, up to 8 cm^2 V^{-1} s^{-1} at room temperature, in uniform, wafer-scale, multilayer films. These films also have charge carrier lifetimes up to 144 ns, or 14× higher than those of previous reports on large-area TMDs. Simulations show that such lifetimes can lead to a solar cell efficiency of ~22.3% and a specific power of ~64 W g^{-1} in a packaged cell, or 3 W g^{-1} in a fully packaged module. These results could facilitate large-scale, commercial TMD solar cells with high specific power, which could address the growing need for lightweight, flexible energy harvesters for applications in IoT, wearables, electric vehicles, and aerospace.

METHODS

Growth. Solid-source selenium selenization was carried out in a two-zone PlanarTech CVD system, with the primary zone consisting of a hatch furnace and the second heating zone consisting of an insulating jacket with heating coils in order to vaporize the solid-source selenium.

Gas-source selenization was performed in a cold-wall rapid thermal processing furnace (Annealsys AS-One 150), capable of housing 150 mm wafers. The heat was provided by infrared halogen lamps on the chamber's lid, and the temperature was monitored using a thermocouple attached to the susceptor. Processing gases were nitrogen and 10% diluted H_2Se in N_2.

Transmission Electron Microscopy. To study the cross-section of the samples, a FIB lamella was prepared from each sample on a Cu Omniprobe TEM grid using a Thermo Fisher Helios FIB-SEM system for characterization. High-angle annular dark-field scanning TEM (HAADF-STEM) and EDS were performed on an aberration-corrected Thermo Fisher Titan transmission electron microscope at 300 kV using a Super X detector. To prevent damage from the ion beam on the sample, the surface was covered with a carbon–platinum layer and then coated with platinum.

Raman Spectroscopy. Raman spectroscopy was taken using a HORIBA LabRAM HR Evolution spectrometer with a laser wavelength of λ = 532 nm at P = 0.5 mW and at 1800 gr/mm, unless otherwise specified.

Atomic Force Microscopy. AFM was taken with a Park NX-10 using an NSC-15 tip at a scan rate of 0.75 Hz.

X-ray Diffraction. XRD was carried out with a PANAnalytical X'Pert 2 diffractometer with a Cu–Kα source. Samples were first aligned to the (400) silicon peak to ensure orientation in the z direction and then measured using Cu–Kα radiation through a 1/2″ slit without a parallel plate collimator.

Time-Resolved Microwave Conductivity. The detailed process for producing a quantitative measurement from TRMC is given in detail in our previous work, Reid et al.[32]

Specific Power Calculation. The specific power was calculated based on the solar cell efficiency and the areal weight densities of the solar cell or module. The output power is equal to efficiency multiplied by the incident power of 100 mW cm^{-2} (AM 1.5 G one sun illumination), and specific power is equal to the output power divided by the areal density. The areal density of the packaged cell was calculated by summing up the areal densities of all materials in the packaged solar cell stack by using the volumetric mass density multiplied by the respective material thickness, as explained in detail in our previous study.[11] A material stack of 1 μm polyimide (substrate), 80 nm gold (back contact/reflector), 26 nm WSe_2 (absorber), single-layer graphene (top contact), and 70 nm MoO_x (antireflection coating/encapsulation layer) was considered as an example device structure.[11] The areal densities of the packaged modules were taken from the literature.[5] The values correspond to a lightweight, all-plastic packaging compatible with moisture-insensitive thin-film solar technologies.

ASSOCIATED CONTENT

Data Availability Statement

The data that support the findings of this study are available from the corresponding author upon reasonable request.

Supporting Information

The Supporting Information is available free of charge at https://pubs.acs.org/doi/10.1021/acsnano.4c03590.

Raman data for varying W sputtering conditions; elemental analysis of WSe_2 films; TEM images of H_2Se films with elemental analysis; fit parameters from XRD; Hall measurements of SS-Se and H_2Se WSe_2; benchmarking; absorbance and steady-state microwave conductivity; and SRH lifetimes (PDF)

AUTHOR INFORMATION

Corresponding Author

Eric Pop − *Department of Electrical Engineering, Stanford University, Stanford, California 94305, United States; Department of Materials Science & Engineering, Stanford University, Stanford, California 94305, United States; Precourt Institute for Energy, Stanford University, Stanford, California 94305, United States;* orcid.org/0000-0003-0436-8534; Email: epop@stanford.edu

Authors

Kathryn M. Neilson − *Department of Electrical Engineering, Stanford University, Stanford, California 94305, United States;* orcid.org/0000-0003-1061-2919

https://doi.org/10.1021/acsnano.4c03590
ACS Nano 2024, 18, 24819−24828

Sarallah Hamtaei − *Hasselt University, Hasselt 3500, Belgium; Imec, Genk 3600, Belgium; EnergyVille, Genk 3600, Belgium;* orcid.org/0000-0002-5458-7068
Koosha Nassiri Nazif − *Department of Electrical Engineering, Stanford University, Stanford, California 94305, United States;* orcid.org/0000-0002-3991-6484
Joshua M. Carr − *University of Colorado Boulder, Materials Science & Engineering Program, Boulder, Colorado 80303, United States*
Sepideh Rahimisheikh − *University of Antwerp, Electron Microscopy for Materials Science (EMAT), Antwerpen 2020, Belgium*
Frederick U. Nitta − *Department of Electrical Engineering, Stanford University, Stanford, California 94305, United States; Department of Materials Science & Engineering, Stanford University, Stanford, California 94305, United States*
Guy Brammertz − *Hasselt University, Hasselt 3500, Belgium; Imec, Genk 3600, Belgium; EnergyVille, Genk 3600, Belgium*
Jeffrey L. Blackburn − *Chemistry and Nanoscience Center, National Renewable Energy Laboratory, Golden, Colorado 80401, United States;* orcid.org/0000-0002-9237-5891
Joke Hadermann − *University of Antwerp, Electron Microscopy for Materials Science (EMAT), Antwerpen 2020, Belgium;* orcid.org/0000-0002-1756-2566
Krishna C. Saraswat − *Department of Electrical Engineering, Stanford University, Stanford, California 94305, United States; Department of Materials Science & Engineering, Stanford University, Stanford, California 94305, United States*
Obadiah G. Reid − *Chemistry and Nanoscience Center, National Renewable Energy Laboratory, Golden, Colorado 80401, United States; Renewable and Sustainable Energy Institute, University of Colorado Boulder, Boulder, Colorado 80303, United States*
Bart Vermang − *Hasselt University, Hasselt 3500, Belgium; Imec, Genk 3600, Belgium; EnergyVille, Genk 3600, Belgium*
Alwin Daus − *Department of Electrical Engineering, Stanford University, Stanford, California 94305, United States; Sensors Laboratory, Department Microsystems Engineering (IMTEK), University Freiburg, Freiburg 79110, Germany*

Complete contact information is available at: https://pubs.acs.org/10.1021/acsnano.4c03590

Author Contributions

[‡‡]K.M.N., S.H., and K.N. contributed equally. K.M.N., S.H., K.N., and A.D. conceived the project. K.M.N. and S.H. performed the growth of WSe_2. S.H. carried out the SEM and EDS measurements on WSe_2 films. S.R. performed the TEM and subsequent EDS measurements. K.M.N. performed Raman, XRD, and AFM characterization of the films. K.N. fabricated the devices and conducted the Hall measurements. K.N. and F.U.N. modeled the solar cell performance. K.N. carried out the specific power calculations. J.C., J.B., and O.R. conducted the TRMC measurements. K.M.N., S.H., and K.N. wrote the manuscript, with assistance from A.D., J.C., S.R., and E.P. E.P. supervised the work. All authors contributed to the data interpretation, presentation, and revision of the manuscript.

Notes

The authors declare no competing financial interest.

ACKNOWLEDGMENTS

K.M.N. acknowledges support from the Stanford Graduate Fellowship (SGF) and from the National Science Foundation Graduate Research Fellowship (NSF-GRFP). S.H. acknowledges financial support from the Flanders Research Foundation (FWO)—strategic basic research doctoral grant 1S31922N. K.N. acknowledges partial support from the Stanford Precourt Institute for Energy and the member companies of the SystemX Alliance at Stanford. A.D. acknowledges support by the Deutsche Forschungsgemeinschaft (DFG, German Research Foundation) through the Emmy Noether Programme (506140715). Part of this work was performed at the Stanford Nano Shared Facilities (SNSF), supported by the National Science Foundation under award ECCS-2026822. Additionally, this work was authored, in part, by the National Renewable Energy Laboratory, operated by Alliance for Sustainable Energy, LLC, for the U.S. Department of Energy (DOE) under Contract no. DE-AC36-08GO28308. Microwave conductivity measurements and analysis at NREL were funded by the Solar Photochemistry Program, Division of Chemical Sciences, Geosciences, and Biosciences, Office of Basic Energy Sciences, U.S. DOE. The views expressed in the article do not necessarily represent the views of the DOE or the U.S. Government.

REFERENCES

(1) Das, S.; Sebastian, A.; Pop, E.; McClellan, C. J.; Franklin, A. D.; Grasser, T.; Knobloch, T.; Illarionov, Y.; Penumatcha, A. V.; Appenzeller, J.; Chen, Z.; Zhu, W.; Asselberghs, I.; Li, L.-J.; Avci, U. E.; Bhat, N.; Anthopoulos, T. D.; Singh, R. Transistors based on two-dimensional materials for future integrated circuits. *Nat. Electron.* **2021**, *4* (11), 786−799.
(2) Jariwala, D.; Davoyan, A. R.; Wong, J.; Atwater, H. A. Van der Waals Materials for Atomically-Thin Photovoltaics: Promise and Outlook. *ACS Photonics* **2017**, *4* (12), 2962−2970.
(3) Daus, A.; Vaziri, S.; Chen, V.; Köroğlu, Ç.; Grady, R. W.; Bailey, C. S.; Lee, H. R.; Schauble, K.; Brenner, K.; Pop, E. High-performance flexible nanoscale transistors based on transition metal dichalcogenides. *Nat. Electron.* **2021**, *4* (7), 495−501.
(4) Kim, K.-H.; Andreev, M.; Choi, S.; Shim, J.; Ahn, H.; Lynch, J.; Lee, T.; Lee, J.; Nazif, K. N.; Kumar, A.; Kumar, P.; Choo, H.; Jariwala, D.; Saraswat, K. C.; Park, J.-H. High-Efficiency WSe_2 Photovoltaic Devices with Electron-Selective Contacts. *ACS Nano* **2022**, *16* (6), 8827−8836.
(5) Reese, M. O.; Glynn, S.; Kempe, M. D.; McGott, D. L.; Dabney, M. S.; Barnes, T. M.; Booth, S.; Feldman, D.; Haegel, N. M. Increasing markets and decreasing package weight for high-specific-power photovoltaics. *Nat. Energy* **2018**, *3* (11), 1002−1012.
(6) Hu, Z.; Lin, D.; Lynch, J.; Xu, K.; Jariwala, D. How good can 2D excitonic solar cells be? *Device* **2023**, *1* (1), 100003.
(7) Went, C. M.; Wong, J.; Jahelka, P. R.; Kelzenberg, M.; Biswas, S.; Hunt, M. S.; Carbone, A.; Atwater, H. A. A new metal transfer process for van der Waals contacts to vertical Schottky-junction transition metal dichalcogenide photovoltaics. *Sci. Adv.* **2019**, *5* (12), No. eaax6061.
(8) Nassiri Nazif, K.; Nitta, F. U.; Daus, A.; Saraswat, K. C.; Pop, E. Efficiency limit of transition metal dichalcogenide solar cells. *Commun. Phys.* **2023**, *6* (1), 367.
(9) Nassiri Nazif, K. Transition Metal Dichalcogenides for Next-Generation Photovoltaics. 2021. https://searchworks.stanford.edu/view/14053731 (accessed June 20, 2024).
(10) Hou, F.; Ren, X.; Guo, H.; Ning, X.; Wang, Y.; Li, T.; Zhu, C.; Zhao, Y.; Zhang, X. Monolithic perovskite/silicon tandem solar cells: A review of the present status and solutions toward commercial application. *Nano Energy* **2024**, *124*, 109476.

(11) Nassiri Nazif, K.; Daus, A.; Hong, J.; Lee, N.; Vaziri, S.; Kumar, A.; Nitta, F.; Chen, M. E.; Kananian, S.; Islam, R.; Kim, K.-H.; Park, J.-H.; Poon, A. S. Y.; Brongersma, M. L.; Pop, E.; Saraswat, K. C. High-specific-power flexible transition metal dichalcogenide solar cells. *Nat. Commun.* **2021**, *12* (1), 7034.
(12) Nakamura, M.; Yamaguchi, K.; Kimoto, Y.; Yasaki, Y.; Kato, T.; Sugimoto, H. Cd-Free Cu(In,Ga)(Se,S)$_2$ Thin-Film Solar Cell With Record Efficiency of 23.35. *IEEE J. Photovolt.* **2019**, *9* (6), 1863−1867.
(13) Huang, J.-K.; Pu, J.; Hsu, C.-L.; Chiu, M.-H.; Juang, Z.-Y.; Chang, Y.-H.; Chang, W.-H.; Iwasa, Y.; Takenobu, T.; Li, L.-J. Large-Area Synthesis of Highly Crystalline WSe_2 Monolayers and Device Applications. *ACS Nano* **2014**, *8* (1), 923−930.
(14) Hynek, D. J.; Onder, E.; Hart, J. L.; Jin, G.; Wang, M.; Singhania, R. M.; Davis, B.; Strandwitz, N. C.; Cha, J. J. Substrate Effects on Growth Dynamics of WTe_2 Thin films. *Adv. Mater. Interfaces* **2023**, *10* (11), 2202397.
(15) Kang, H.; Yun, S. J.; Jung, K. H.; Lim, J. W. Multi-wafer-scale growth of WSe_2 films using a traveling flow-type reactor with a remote thermal Se cracker. *Appl. Surf. Sci.* **2020**, *528*, 146951.
(16) Lin, W.-S.; Medina, H.; Su, T.-Y.; Lee, S.-H.; Chen, C.-W.; Chen, Y.-Z.; Manikandan, A.; Shih, Y.-C.; Yang, J.-H.; Chen, J.-H.; Wu, B.-W.; Chu, K.-W.; Chuang, F.-C.; Shieh, J.-M.; Shen, C.-H.; Chueh, Y.-L. Selection Role of Metal Oxides into Transition Metal Dichalcogenide Monolayers by a Direct Selenization Process. *ACS Appl. Mater. Interfaces* **2018**, *10* (11), 9645−9652.
(17) Hussain, S.; Patil, S. A.; Vikraman, D.; Arbab, A. A.; Jeong, S. H.; Kim, H.-S.; Jung, J. Growth of a WSe_2/W counter electrode by sputtering and selenization annealing for high-efficiency dye-sensitized solar cells. *Appl. Surf. Sci.* **2017**, *406*, 84−90.
(18) Li, H.; Gao, D.; Xie, S.; Zou, J. Effect of magnetron sputtering parameters and stress state of W film precursors on WSe_2 layer texture by rapid selenization. *Sci. Rep.* **2016**, *6* (1), 36451.
(19) Morabito, F.; Synnatschke, K.; Mehew, J. D.; Varghese, S.; Sayers, C. J.; Folpini, G.; Petrozza, A.; Cerullo, G.; Tielrooij, K.-J.; Coleman, J.; Nicolosi, V.; Gadermaier, C. Long lived photogenerated charge carriers in few-layer transition metal dichalcogenides obtained from liquid phase exfoliation. *Nanoscale Adv.* **2024**, *6*, 1074−1083.
(20) Jäger-Waldau, A.; Bucher, E. WSe_2 thin films prepared by soft selenization. *Thin Solid Films* **1991**, *200* (1), 157−164.
(21) Hei, J.; Li, X.; Wu, S.; Lin, P.; Shi, Z.; Tian, Y.; Li, X.; Zeng, L.; Yu, X.; Wu, D. Wafer-Scale Patterning Synthesis of Two-Dimensional WSe_2 Layers by Direct Selenization for Highly Sensitive van der Waals Heterojunction Broadband Photodetectors. *ACS Appl. Mater. Interfaces* **2023**, *15* (9), 12052−12060.
(22) Aftab, S.; Iqbal, M. Z.; Hussain, S.; Hegazy, H. H.; Saeed, M. A. Transition metal dichalcogenides solar cells and integration with perovskites. *Nano Energy* **2023**, *108*, 108249.
(23) Hamtaei, S.; Brammertz, G.; Kohl, T.; Buldu, D. G.; Birant, G.; de Wild, J.; Meuris, M.; Poortmans, J.; Vermang, B. Investigating the experimental space for two-step Cu(In,Ga)(S,Se)$_2$ absorber layer fabrication: A design of experiment approach. *Thin Solid Films* **2021**, *738*, 138958.
(24) Vleuten, M. v. d.; Theelen, M.; Aninat, R.; Werf, K. v. d.; Mannetje, H.; Reyes-Figueroa, P.; Kodalle, T.; Klenk, R.; Simor, M.; Linden, H. In Control over the Gallium Depth Profile in 30 × 30 cm^2 Sequentially Processed CIGS. In *2020 47th IEEE Photovoltaic Specialists Conference (PVSC)*, 2020; pp 0640−0645.
(25) Zeng, W.; Feng, L.-P.; Su, J.; Pan, H.-x.; Liu, Z.-T. Layer-controlled and atomically thin WS_2 films prepared by sulfurization of atomic-layer-deposited WO_3 films. *J. Alloys Compd.* **2018**, *745*, 834−839.
(26) Zhou, D.; Shu, H.; Hu, C.; Jiang, L.; Liang, P.; Chen, X. Unveiling the Growth Mechanism of MoS_2 with Chemical Vapor Deposition: From Two-Dimensional Planar Nucleation to Self-Seeding Nucleation. *Cryst. Growth Des.* **2018**, *18* (2), 1012−1019.
(27) Schutte, W. J.; De Boer, J. L.; Jellinek, F. Crystal structures of tungsten disulfide and diselenide. *J. Solid State Chem.* **1987**, *70* (2), 207−209.
(28) Patterson, A. L. The Scherrer Formula for X-Ray Particle Size Determination. *Phys. Rev.* **1939**, *56* (10), 978−982.
(29) del Corro, E.; Terrones, H.; Elias, A.; Fantini, C.; Feng, S.; Nguyen, M. A.; Mallouk, T. E.; Terrones, M.; Pimenta, M. A. Excited Excitonic States in 1L, 2L, 3L, and Bulk WSe_2 Observed by Resonant Raman Spectroscopy. *ACS Nano* **2014**, *8* (9), 9629−9635.
(30) Qian, Q.; Peng, L.; Perea-Lopez, N.; Fujisawa, K.; Zhang, K.; Zhang, X.; Choudhury, T. H.; Redwing, J. M.; Terrones, M.; Ma, X.; Huang, S. Defect creation in WSe_2 with a microsecond photoluminescence lifetime by focused ion beam irradiation. *Nanoscale* **2020**, *12* (3), 2047−2056.
(31) Dadgar, A. M.; Scullion, D.; Kang, K.; Esposito, D.; Yang, E. H.; Herman, I. P.; Pimenta, M. A.; Santos, E. J. G.; Pasupathy, A. N. Strain Engineering and Raman Spectroscopy of Monolayer Transition Metal Dichalcogenides. *Chem. Mater.* **2018**, *30* (15), 5148−5155.
(32) Reid, O. G.; Moore, D. T.; Li, Z.; Zhao, D.; Yan, Y.; Zhu, K.; Rumbles, G. Quantitative analysis of time-resolved microwave conductivity data. *J. Phys. D: Appl. Phys.* **2017**, *50* (49), 493002.
(33) Labram, J. G.; Perry, E. E.; Venkatesan, N. R.; Chabinyc, M. L. Steady-state microwave conductivity reveals mobility-lifetime product in methylammonium lead iodide. *Appl. Phys. Lett.* **2018**, *113* (15), 153902.
(34) Blackburn, J. L.; Zhang, H.; Myers, A. R.; Dunklin, J. R.; Coffey, D. C.; Hirsch, R. N.; Vigil-Fowler, D.; Yun, S. J.; Cho, B. W.; Lee, Y. H.; Miller, E. M.; Rumbles, G.; Reid, O. G. Measuring Photoexcited Free Charge Carriers in Mono- to Few-Layer Transition-Metal Dichalcogenides with Steady-State Microwave Conductivity. *J. Phys. Chem. Lett.* **2020**, *11* (1), 99−107.
(35) Bindl, D. J.; Ferguson, A. J.; Wu, M.-Y.; Kopidakis, N.; Blackburn, J. L.; Arnold, M. S. Free Carrier Generation and Recombination in Polymer-Wrapped Semiconducting Carbon Nanotube Films and Heterojunctions. *J. Phys. Chem. Lett.* **2013**, *4* (21), 3550−3559.
(36) Park, J.; Reid, O. G.; Rumbles, G. Photoinduced Carrier Generation and Recombination Dynamics of a Trilayer Cascade Heterojunction Composed of Poly(3-hexylthiophene), Titanyl Phthalocyanine, and C60. *J. Phys. Chem. B* **2015**, *119* (24), 7729−7739.
(37) Ferguson, A. J.; Kopidakis, N.; Shaheen, S. E.; Rumbles, G. Dark Carriers, Trapping, and Activation Control of Carrier Recombination in Neat P3HT and P3HT:PCBM Blends. *J. Phys. Chem. C* **2011**, *115* (46), 23134−23148.
(38) Ihly, R.; Mistry, K. S.; Ferguson, A. J.; Clikeman, T. T.; Larson, B. W.; Reid, O.; Boltalina, O. V.; Strauss, S. H.; Rumbles, G.; Blackburn, J. L. Tuning the driving force for exciton dissociation in single-walled carbon nanotube heterojunctions. *Nat. Chem.* **2016**, *8* (6), 603−609.
(39) Li, Y.; Chernikov, A.; Zhang, X.; Rigosi, A.; Hill, H. M.; van der Zande, A. M.; Chenet, D. A.; Shih, E.-M.; Hone, J.; Heinz, T. F. Measurement of the optical dielectric function of monolayer transition-metal dichalcogenides: MoS_2, $MoSe_2$, WS_2 and WSe_2. *Phys. Rev. B* **2014**, *90* (20), 205422.
(40) Dicker, G.; de Haas, M. P.; Siebbeles, L. D. A.; Warman, J. M. Electrodeless time-resolved microwave conductivity study of charge-carrier photogeneration in regioregular poly(3-hexylthiophene) thin films. *Phys. Rev. B* **2004**, *70* (4), 045203.
(41) Ferguson, A. J.; Kopidakis, N.; Shaheen, S. E.; Rumbles, G. Quenching of Excitons by Holes in Poly(3-hexylthiophene) Films. *J. Phys. Chem. C* **2008**, *112* (26), 9865−9871.
(42) Ando, Y.; Khatri, I.; Matsumori, H.; Sugiyama, M.; Nakada, T. Epitaxial Cu(In,Ga)Se_2 Thin Films on Mo Back Contact for Solar Cells. *Phys. Status Solidi A* **2019**, *216* (16), 1900164.
(43) Ochoa, M.; Buecheler, S.; Tiwari, A. N.; Carron, R. Challenges and opportunities for an efficiency boost of next generation Cu(In,Ga)Se_2 solar cells: prospects for a paradigm shift. *Energy Environ. Sci.* **2020**, *13* (7), 2047−2055.
(44) Ablekim, T.; Duenow, J. N.; Perkins, C. L.; Moseley, J.; Zheng, X.; Bidaud, T.; Frouin, B.; Collin, S.; Reese, M. O.; Amarasinghe, M.; Colegrove, E.; Johnston, S.; Metzger, W. K. Exceeding 200 ns

https://doi.org/10.1021/acsnano.4c03590
ACS Nano 2024, 18, 24819−24828

Lifetimes in Polycrystalline CdTe Solar Cells. *Sol. RRL* **2021**, *5* (8), 2100173.
(45) Jakubowicz, A.; Mahalu, D.; Wolf, M.; Wold, A.; Tenne, R. WSe_2: Optical and electrical properties as related to surface passivation of recombination centers. *Phys. Rev. B* **1989**, *40* (5), 2992−3000.

https://doi.org/10.1021/acsnano.4c03590
ACS Nano 2024, 18, 24819−24828

Supporting Information

Toward Mass Production of Transition Metal Dichalcogenide Solar Cells: Scalable Growth of Photovoltaic-Grade Multilayer WSe_2 by Tungsten Selenization

Kathryn M. Neilson,[1†] Sarallah Hamtaei,[2,3,4†] Koosha Nassiri Nazif,[1†] Joshua M. Carr,[5] Sepideh Rahimisheikh,[6] Frederick U. Nitta,[1,7] Guy Brammertz,[2,3,4] Jeffrey L. Blackburn,[8] Joke Hadermann,[6] Krishna C. Saraswat,[1,7] Obadiah G. Reid,[8,9] Bart Vermang,[2,3,4] Alwin Daus,[1,10] and Eric Pop[1,7,11]

[1]*Dept. of Electrical Engineering, Stanford Univ., Stanford, CA 94305, USA*
[2]*Hasselt Univ., imo-imomec, Hasselt 3500, Belgium*
[3]*Imec, imo-imomec, Genk 3600, Belgium*
[4]*EnergyVille, imo-imomec, Genk 3600, Belgium*
[5]*Univ. of Colorado Boulder, Materials Science & Engineering Program, Boulder CO 80303, USA*
[6]*Univ. of Antwerp, Electron Microscopy for Materials Science (EMAT), Antwerpen 2020, Belgium*
[7]*Dept. of Materials Science & Engineering, Stanford Univ., Stanford, CA 94305, USA*
[8]*National Renewable Energy Laboratory, Chemistry and Nanoscience Center, Golden CO 80401, USA*
[9]*University of Colorado Boulder, Renewable and Sustainable Energy Institute, Boulder CO 80303, USA*
[10]*Sensors Laboratory, Dept. Microsystems Engineering (IMTEK), Univ. Freiburg, Freiburg, Germany*
[11]*Precourt Institute for Energy, Stanford Univ., Stanford, CA 94305, USA*

[†]*These authors contributed equally. *Corresponding author email: epop@stanford.edu*

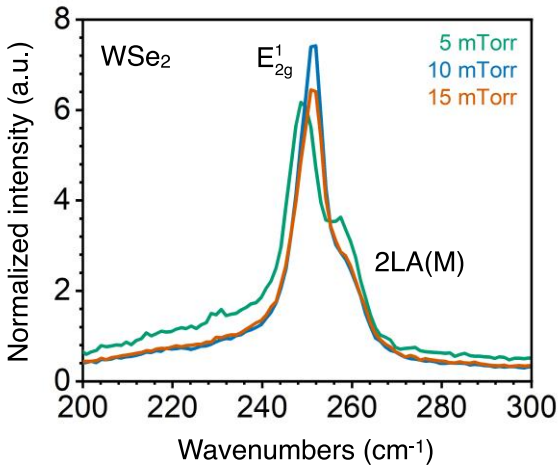

Supporting Information Fig. 1: Finding the optimal W sputtering pressure via Raman spectroscopy. The figure shows Raman spectra of as-grown WSe_2 with the starting W film sputtered at varying pressures. In order to optimize the W sputtering pressure, 10 nm films of W were sputtered at 5, 10, and 15 mTorr and subsequently grown using the same recipe as described in the main text. To determine an optimal W sputtering condition, we selenize W films deposited at three sputtering pressures and compare the intensity of the E^1_{2g}/A_{1g} peak to the 2LA(M) signature in WSe_2. The 2LA(M) vibrational mode is thought to become active due to structure disorder,[1] therefore we compare the defect-related signature intensity to that of the E^1_{2g} and A_{1g} phonon mode. From this, it can be seen that a pressure of 10 mTorr gives the highest E^1_{2g}/A_{1g} intensity. Increasing sputtering pressures generally allow for more porosity in the film, but too much porosity could lead to a non-homogeneous film. Therefore, we believe that 10 mTorr could act as a balance between these two competing factors.

Supporting Information Table 1: Full analysis of WSe_2 films' elemental composition by energy dispersive x-ray spectroscopy (EDS). In each sample, the mean and coefficient of variation (CV) is reported for three different measurements. Note that there is a carbon peak reported in all cases, which is a well-known contaminant in EDS analysis; any residual organic gases in the measurement chamber (or with the sample itself) is exposed to, and cracked by, the electron beam, and subsequently reflected in the response as carbon peak. As expected, this is further intensified for samples transferred onto PI. The source of oxygen can also be attributed to leftover oxygen in the chamber, or native oxides.

Sample		*Statistics*	*Atomic concentration (%)*					*Ratio*
			C	*O*	*Si*	*Se*	*W*	*Se/W*
On silicon	**SS-Se**	*Mean*	5.24	3.39	76.88	**10.10**	**4.39**	**2.29**
		CV (%)	1.31	10.04	0.66	**2.60**	**0.85**	**1.93**
	H_2Se	*Mean*	4.54	1.61	81.14	**8.26**	**4.45**	**1.85**
		CV (%)	3.23	9.85	0.54	**2.79**	**1.01**	**2.84**
On polyimide	**SS-Se**	*Mean*	70.22	14.97	-	**10.23**	**4.59**	**2.22**
		CV (%)	1.08	5.27	-	**0.95**	**1.32**	**2.26**
	H_2Se	*Mean*	70.85	14.91	-	**9.77**	**4.47**	**2.18**
		CV (%)	1.13	6.39	-	**0.84**	**1.71**	**1.08**

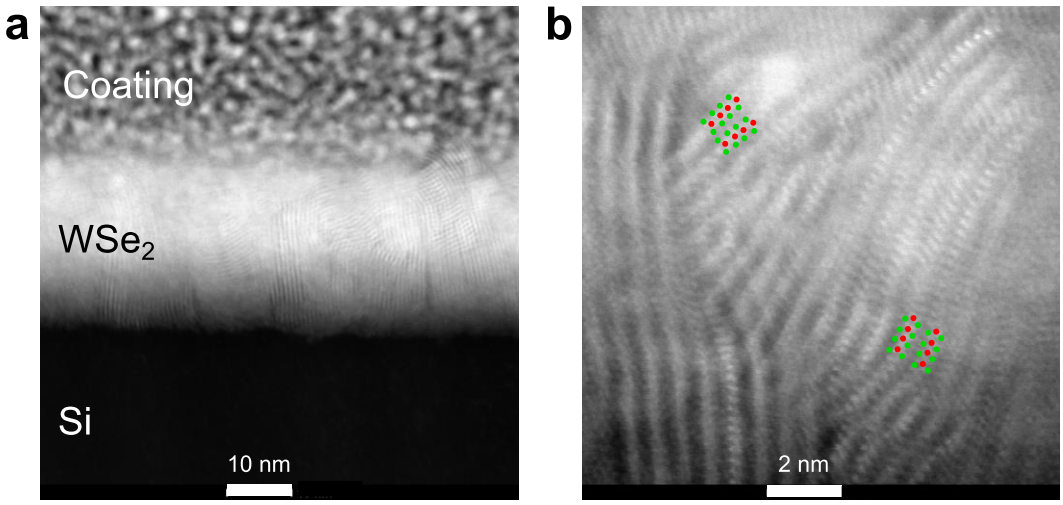

Supporting Information Fig. 2: Transmission electron microscopy (TEM) of H_2Se-selenized films. a, Cross-sectional view of selenized films on a silicon substrate with a metallic coating. **b,** A higher magnification image showing the varied orientation of lamella. The H_2Se-selenized films are prepared as described in Methods section within the main text. Films show varied orientations, unlike the exclusively (00ℓ) orientation from solid source grown films shown in **Fig. 3d**. This corroborates the orientations seen in X-ray diffraction measurement (**Fig. 3h**). Further optimization of the growth parameters could further reduce the vertical orientation.[2]

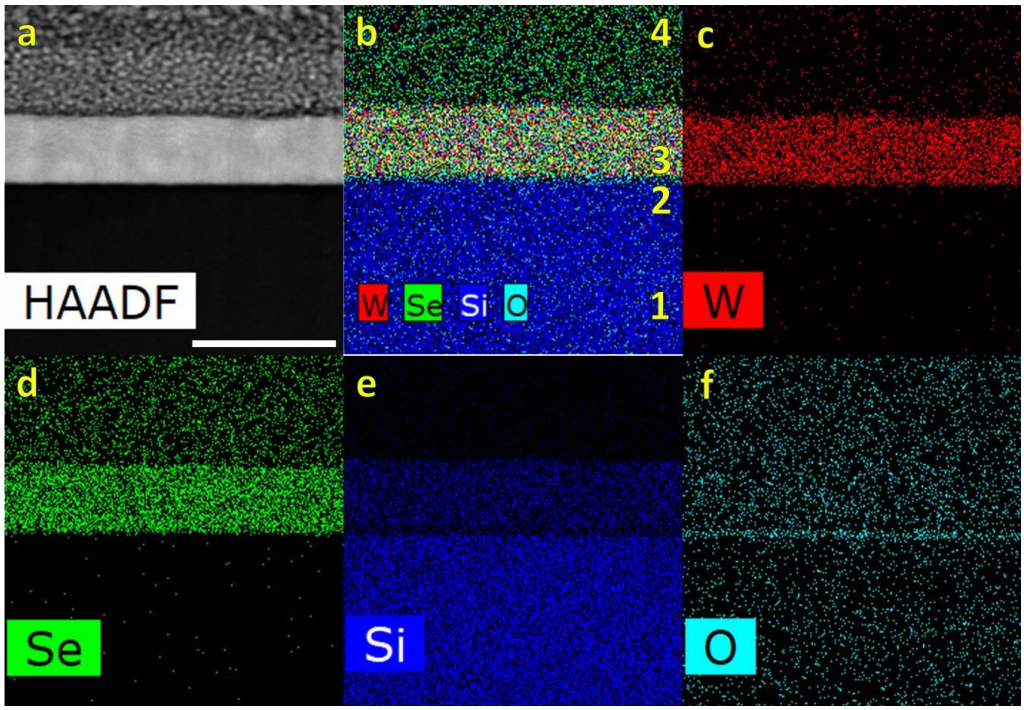

Supporting Information Fig. 3: Elemental mapping of H_2Se-selenized films using Energy Dispersive X-Ray Spectroscopy. a, HAADF-STEM cross-section. Scale bar, 60 nm. **b**, the overlap of the elemental maps. Regions 1, 2, 3, and 4 refer to Si, SiO_2, WSe_2, and Pt-C protective layer, respectively. **c-f**, The elemental distribution of **c**, W, **d**, Se, **e**, Si, and **f**, O, respectively. All images are at the same scale.

Supporting Information Note 1. Method of extracting grain sizes from X-ray diffraction measurements

Grain sizes and micro strain analysis are estimated using the Scherrer equation (**Supporting Information Equation 1**) by fitting a Gaussian curve to the (002) diffraction peak in both solid source and H_2Se-selenized films. Subsequent estimated grain sizes can be found in **Supporting Information Table 2.**

$$D = \frac{K \cdot \lambda}{FWHM \cdot \cos(\theta)} \quad (1)$$

Where:

D = Crystallite or grain size

K = Scherrer shape factor, typically around 0.9 (Ref. 3)

λ = Cu-Kα wavelength (1.54 Å)

FWHM = Full width at half maximum at the diffraction peak

θ = Bragg angle of diffraction at a given peak

Supporting Information Table 2: Fit and calculated parameters from x-ray diffraction analysis.

Film	2θ (°)	FWHM (°)	Grain Size (nm)	Strain
H_2Se	13.16	0.978	8	3.5%
SS-Se	13.62	0.478	17	0.02%

Strain is calculated using lattice spacing reported in the ICSD database, where *d* is the calculated lattice spacing from XRD and d_0 is the theoretical lattice spacing (**Supporting Information Equation 2**). The theoretical lattice spacing is taken from the ICSD database[4] to estimate strain, although further un-idealities of the measurement can be included for a more precise value.

$$Strain\ (\%) = \frac{d - d_0}{d_0} \cdot 100 \quad (2)$$

Supporting Information Note 2. Method of extracting Hall mobility in selenized WSe_2 films

Square WSe_2 samples having four contacts are prepared for the van der Pauw method to determine the majority carrier type, obtain the Hall mobility and density of majority carrier in the films using a DC Hall effect measurement System (Lakeshore 8404). The van der Pauw method is preferred as other field-effect type mobility measurements can suffer from inaccurate extractions due to an underestimated threshold voltage and contact resistance,[5] both of which require further optimization. The measurement is performed on ~26 nm-thick WSe_2 films from SS-Se (and ~27-nm thick H_2Se WSe_2 films) transferred onto flexible insulating ~5 μm-thick polyimide substrates (**Supporting Information Fig. 4a**). Four 2 mm × 2 mm gold (Au) contact pads are e-beam evaporated on top of the WSe_2 film in a square van der Pauw pattern with a side length of 10 mm (**Supporting Information Fig. 4b**), which according to the tool's manual results in a measurement error less than 2%.

Hole mobilities of 8.1 $cm^2\ V^{-1}\ s^{-1}$ (5.5 $cm^2\ V^{-1}\ s^{-1}$) and densities of $1.6 \times 10^{17}\ cm^{-3}$ ($4.2 \times 10^{17}\ cm^{-3}$) are measured by the Hall effect in H_2Se (SS-Se) films, respectively. Note that the maximum Hall mobility is obtained from H_2Se growth, while SS-Se growth leads to higher carrier density. These are among the best mobility results reported to date for selenized WSe_2 (**Supporting Information Table 2**). SS-Se samples have a tight distribution of Hall mobility and hole density, but H_2Se samples show wider variation. This could be explained by the mobility anisotropy in WSe_2 and the random orientation of WSe_2 layers observed in the H_2Se growth (**Supporting Information Fig. 2**), leading to sample-to-sample variation, as opposed to SS-Se growth, which mostly consists of horizontally oriented WSe_2 layers exhibiting in-plane mobility.

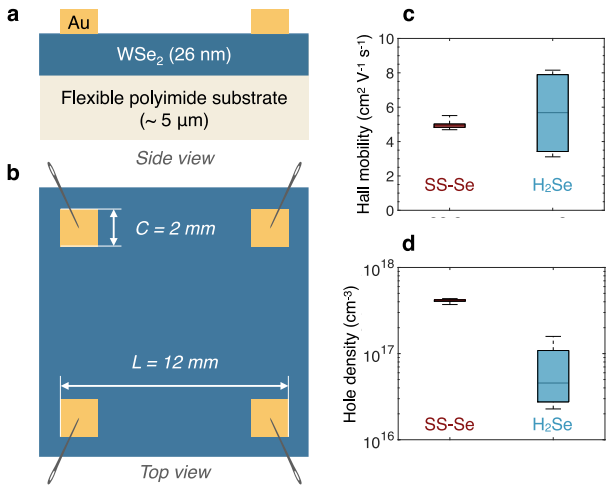

Supporting Information Fig. 4: Van der Pauw measurements to determine Hall mobility, majority carrier type and majority carrier density of WSe_2 films. a, side view and **b,** top view of the square four-contact van der Pauw structure used to measure the Hall mobility, majority carrier type (i.e., holes) and hole density. **c,** Hall mobility and **d,** hole density of WSe_2 grown by selenization of tungsten in solid-source selenium (SS-Se) and H_2Se furnaces. Hall mobilities as high as 8 $cm^2\ V^{-1}\ s^{-1}$ are demonstrated in the H_2Se-based films, and a maximum hole density of $4.2 \times 10^{17}\ cm^{-3}$ is measured in the SS-Se films.

Supporting Information Table 2. Our selenization growth methods vs. existing reports. All mobility measurements are at room temperature, unless stated otherwise.

Author	Growth method	WSe_2 thickness	Mobility ($cm^2V^{-1}s^{-1}$)	Mobility measurement method	Grain size (nm)	Film uniform?	Carrier lifetime (ns)	Growth temp. (°C)	Growth time (hrs)
SS-Se (this work)	W selenization	22 nm	Up to 5	Hall Effect	17	Yes	144	<900	>2
H_2Se *(this work)*	W selenization	22 nm	Up to 8	Hall Effect	8	Yes	100	<650	>1
Campbell *et al.*[6]	W/WO_3 selenization	2.5 nm	10	Field effect (V_T improperly extracted)	400	No	—	<800	>1.5
Kang *et al.*[7]	W selenization	6 nm	0.15 [FE] 22.8 [Hall]	Field effect (FE) & Hall effect	—	Yes	—	<600	—
Jäger-Waldau *et al.*[8]	W selenization on quartz	400 nm to 4 μm	—	—	10-35	No	—	<850	>18
Li *et al.*[9]	W selenization	25-200 nm	—	—	—	No	—	<600	>1
Hussain *et al.*[10]	W selenization	—	—	—	—	No	—	<600	>1
Medina *et al.*[11]	WO_x selenization	5 nm	6	Hall effect	—	Yes	—	<500	>2
Ma *et al.*[12]	W selenization	100 nm (W)	30	Hall effect	80	No	—	<900	>20
Salitra *et al.*[13]	WO_3 selenization	2 μm (WO_3)	—	—	10-100	No	—	<950	>1
Browning *et al.*[14]	WO_3 selenization	<10 nm	—	—	50-200	Yes	—	<900	—
Kadiwala *et al.*[15]	W/WO_3 selenization	3-40 nm	—	—	—	No	—	<850	20 min

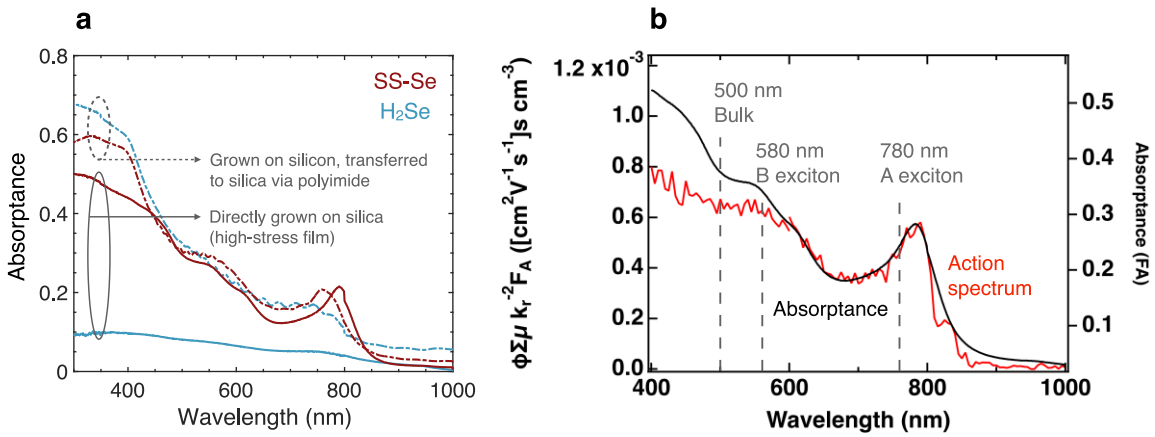

Supporting Information Fig. 5: Optical absorptance and steady-state microwave conductivity (SSMC) measurements to determine excitation wavelengths used in Flash-photolysis time-resolved microwave conductivity (TRMC). a, Optical absorptance of SS-Se and H_2Se WSe_2 films used in this study collected in a center-mounted configuration to account for reflection and transmission components simultaneously. **b,** SSMC action spectrum and optical absorption spectrum of SS-Se films. By first examining the optical absorption and action spectrum we can determine at what excitation wavelengths the TRMC experiments can be conducted to look for differences in the physical processes present in the optical absorption.

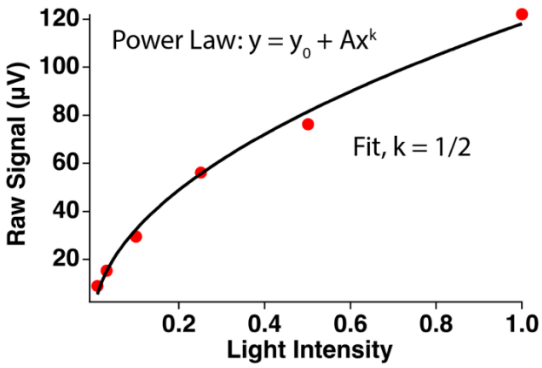

Supporting Information Fig. 6: Raw steady state microwave conductivity (SSMC) versus light intensity. Plot of raw signal from the SSMC measurement for the SS-Se films versus incident light intensity. The light intensity is attenuated by addition of neutral density filters just before the entrance slit into the microwave cavity. Fitting the raw signal curve as a function of light intensity with a power law provides a molecularity relationship that demonstrates a square-root dependence, indicative of a bimolecular (second-order) recombination process which dominates the SSMC signal in the above figure. Fitting the raw signal curve as a function of light intensity with a power law provides a molecularity relationship that demonstrates a square-root dependence, indicative of a bimolecular (second-order) recombination process which dominates the SSMC signal in the above figure. Assuming that the excitation density in the SSMC is not approaching the trap density in these experiments, this observation is consistent with an SRH recombination dominated process with respect to the recombination loss. This molecularity fit is used in the SSMC analysis to ensure that the conductivity units for the y-axis are correct, particularly that the radiative recombination rate constant, k_r, is appropriately accounted for in the raw signal for calculating the action spectrum.

Supporting Information Table 3: Practical performance limits of 26 nm-thick WSe_2 solar cells at various material quality levels, as represented by Shockley-Reed-Hall (SRH) lifetimes, τ_{SRH}. The limits are calculated using a detailed balance model developed by Nassiri Nazif et al.,[16] which incorporates measured optical absorption spectra and includes radiative, Auger, and defect-assisted SRH recombination mechanisms. WSe_2 solar cells made from our selenized WSe_2 films, which have τ_{SRH} of up to 144 ns, can in practice achieve 22.3% power conversion efficiency upon design optimization. Short-circuit current density; V_{OC}, open-circuit voltage; FF, fill factor; PCE, power conversion efficiency, MPP, maximum power point.

τ_{SRH}	**10 ns**	**100 ns**	**144 ns**	**1 µs**	**∞ (no SRH recombination)**
J_{SC} (mA cm^{-2})	31.0	31.0	31.0	31.0	31.0
V_{OC} (V)	771	890	909	1005	1065
Fill factor	0.76	0.79	0.79	0.81	0.89
V_{MPP} (mV)	637	749	766	860	976
J_{MPP} (mA cm^{-2})	28.7	29.0	29.0	29.2	30.2
PCE (%)	**18.2**	**21.7**	**22.3**	**25.1**	**29.5**

Supporting Information References:

1. Del Corro, E.; Terrones, H.; Elias, A.; Fantini, C.; Feng, S.; Nguyen, M. A.; Mallouk, T. E.; Terrones, M.; Pimenta, M. A., Excited Excitonic States in 1L, 2L, 3L, and Bulk WSe_2 Observed by Resonant Raman Spectroscopy. *ACS Nano* **2014,** *8* (9), 9629-9635.
2. Yue, R.; Nie, Y.; Walsh, L. A.; Addou, R.; Liang, C.; Lu, N.; Barton, A. T.; Zhu, H.; Che, Z.; Barrera, D.; Cheng, L.; Cha, P.-R.; Chabal, Y. J.; Hsu, J. W. P.; Kim, J.; Kim, M. J.; Colombo, L.; Wallace, R. M.; Cho, K.; Hinkle, C. L., Nucleation and growth of WSe_2: enabling large grain transition metal dichalcogenides. *2D Materials* **2017,** *4* (4), 045019.
3. Patterson, A. L., The Scherrer Formula for X-Ray Particle Size Determination. *Physical Review* **1939,** *56* (10), 978-982.
4. Schutte, W. J.; De Boer, J. L.; Jellinek, F., Crystal structures of tungsten disulfide and diselenide. *Journal of Solid State Chemistry* **1987,** *70* (2), 207-209.
5. Nasr, J. R.; Schulman, D. S.; Sebastian, A.; Horn, M. W.; Das, S., Mobility Deception in Nanoscale Transistors: An Untold Contact Story. *Advanced Materials* **2019,** *31* (2), 1806020.
6. Campbell, P. M.; Tarasov, A.; Joiner, C. A.; Tsai, M.-Y.; Pavlidis, G.; Graham, S.; Ready, W. J.; Vogel, E. M., Field-effect transistors based on wafer-scale, highly uniform few-layer p-type WSe_2. *Nanoscale* **2016,** *8* (4), 2268-2276.
7. Kang, H.; Yun, S. J.; Jung, K. H.; Lim, J. W., Multi-wafer-scale growth of WSe_2 films using a traveling flow-type reactor with a remote thermal Se cracker. *Applied Surface Science* **2020,** *528*, 146951.
8. Jäger-Waldau, A.; Bucher, E., WSe_2 thin films prepared by soft selenization. *Thin Solid Films* **1991,** *200* (1), 157-164.
9. Li, H.; Gao, D.; Xie, S.; Zou, J., Effect of magnetron sputtering parameters and stress state of W film precursors on WSe_2 layer texture by rapid selenization. *Scientific Reports* **2016,** *6* (1), 36451.
10. Hussain, S.; Patil, S. A.; Vikraman, D.; Arbab, A. A.; Jeong, S. H.; Kim, H.-S.; Jung, J., Growth of a WSe_2/W counter electrode by sputtering and selenization annealing for high-efficiency dye-sensitized solar cells. *Applied Surface Science* **2017,** *406*, 84-90.
11. Medina, H.; Li, J.-G.; Su, T.-Y.; Lan, Y.-W.; Lee, S.-H.; Chen, C.-W.; Chen, Y.-Z.; Manikandan, A.; Tsai, S.-H.; Navabi, A.; Zhu, X.; Shih, Y.-C.; Lin, W.-S.; Yang, J.-H.; Thomas, S. R.; Wu, B.-W.; Shen, C.-H.; Shieh, J.-M.; Lin, H.-N.; Javey, A.; Wang, K. L.; Chueh, Y.-L., Wafer-Scale Growth of WSe_2 Monolayers Toward Phase-Engineered Hybrid WO_x/WSe_2 Films with Sub-ppb NO_x Gas Sensing by a Low-Temperature Plasma-Assisted Selenization Process. *Chem. Materials* **2017,** *29* (4), 1587-1598.
12. Ma, Q.; Kyureghian, H.; Banninga, J. D.; Ianno, N. J., Thin Film WSe_2 for Use as a Photovoltaic Absorber Material. *MRS Online Proceedings Library (OPL)* **2014,** *1670*, mrss14-1670-e01-02.
13. Salitra, G.; Hodes, G.; Klein, E.; Tenne, R., Highly oriented WSe_2 thin films prepared by selenization of evaporated WO_3. *Thin Solid Films* **1994,** *245* (1), 180-185.
14. Browning, P.; Eichfeld, S.; Zhang, K.; Hossain, L.; Lin, Y.-C.; Wang, K.; Lu, N.; Waite, A. R.; Voevodin, A. A.; Kim, M.; Robinson, J. A., Large-area synthesis of WSe_2 from WO_3 by selenium–oxygen ion exchange. *2D Materials* **2015,** *2* (1), 014003.
15. Kadiwala, K.; Butanovs, E.; Ogurcovs, A.; Zubkins, M.; Polyakov, B., Comparative study of WSe_2 thin films synthesized via pre-deposited WO_3 and W precursor material selenization. *Journal of Crystal Growth* **2022,** *593*, 126764.
16. Nassiri Nazif, K.; Nitta, F.; Daus, A.; Saraswat, K.; Pop, E., Efficiency Limit of Transition Metal Dichalcogenide Solar Cells. *Commun Phys* **2023,** 6, 367.